Proceedings of the ASME 2019
Dynamic Systems and Control Conference
DSCC2019
October 8-11, 2019, Park City, Utah, USA

DSCC2019-9151

TEMPERATURE CONTROL TO REDUCE CAPACITY MISMATCH IN PARALLEL-CONNECTED LITHIUM ION CELLS

Mayank Garg
Research Assistant
Dept. of Mechanical and Nuclear Eng.
The Pennsylvania State University
University Park, Pennsylvania 16802
mxg1042@psu.edu

Tanvir R. Tanim
Battery R&D Scientist
Idaho National Laboratory,
Energy Storage and Advanced Vehicles
Idaho Falls, Idaho
Tanvir.Tanim@inl.gov

Christopher D. Rahn
Professor
Dept. of Mechanical and Nuclear Eng.
The Pennsylvania State University
University Park, Pennsylvania 16802
cdrahn@psu.edu

Hanna Bryngelsson
ESS Performance & Cell Specialist
Volvo Group Trucks Technology
Goteborg, Sweden

Niklas Legnedahl
Senior Technical Specialist
China Euro Vehicle Technology AB
Goteborg, Sweden

ABSTRACT

The temperature and capacity of individual cells affect the current distribution in a battery pack. Non uniform current distribution among parallel-connected cells can lead to capacity imbalance and premature aging. This paper develops models that calculate the current in parallel-connected cells and predict their capacity fade. The model is validated experimentally for a nonuniform battery pack at different temperatures. The paper also proposes and validates the hypothesis that temperature control can reduce capacity mismatch in parallel-connected cells. Three Lithium Iron Phosphate cells, two cells at higher initial capacity than the third cell, are connected in parallel. The pack is cycled for 1500 Hybrid Electric Vehicles cycles with the higher capacity cells regulated at $40°C$ and the lower capacity cell at $20°C$. As predicted by the model, the higher capacity and temperature cells age faster, reducing the capacity mismatch by 48% over the 1500 cycles. A case study shows that cooling of low capacity cells can reduce capacity mismatch and extend pack life.

1 Introduction

Li-ion batteries have higher volumetric and specific energy density, making battery packs smaller and lighter compared to other battery technologies. They are currently a market leader in battery technology with a wide ranging applications from medical devices to power tools, home appliances to grid-level energy storage, and cell phones to electric vehicles (EVs). In the automobile industry, improving fuel efficiency and reducing emissions are driving the adoption of electric powertrains. Transportation accounts for 26% of U.S. greenhouse gas emission and 57% of nitrogen oxide emissions [1], and EVs and hybrid electric vehicles (HEVs) can help to reduce environmental impacts. The safe and efficient operation of lithium-ion batteries are critical for the wider acceptance of vehicle electrification.

Lithium Iron Phosphate (LFP) batteries have stable cathodes due to their olivine crystal structure. The Solid electrolyte interphase (SEI) layer growth on the graphite electrode is a major degradation mechanism in LFP cells [6, 20, 21]. Tanim et al. [26] developed a battery degradation model based on SEI layer growth and validated the model for a single cell degradation. The model is based on the controlled oriented models developed

TABLE 1: ESPM Model Equations [27]

Reaction	Equation	Boundary conditions
Solid phase Li^+ conservation	$\frac{\partial c_s}{\partial t} = \frac{D_s}{r^2}\frac{\partial}{\partial r}\left(r^2\frac{\partial c_s}{\partial r}\right)$	$\left.\frac{\partial c_s}{\partial x}\right\|_{r=0} = 0, -D_s\left.\frac{\partial c_s}{\partial x}\right\|_{r=R_s} = \frac{j^{Li}}{a_s F}$
Solid phase charge conservation	$\frac{\partial}{\partial x}\left(\sigma^{eff}\frac{\partial}{\partial x}\phi_s\right) = j^{Li}$	$-\sigma^{eff}\left.\frac{\partial \phi_s}{\partial x}\right\|_{x=0} = \sigma^{eff}\left.\frac{\partial \phi_s}{\partial x}\right\|_{x=L} = \frac{I}{A}$, $\left.\frac{\partial \phi_s}{\partial x}\right\|_{x=L_n} = \left.\frac{\partial \phi_s}{\partial x}\right\|_{x=L_n+L_s} = 0$
Electrolyte phase Li^+ conservation	$\frac{\partial(\varepsilon_e c_e)}{\partial t} = \frac{\partial}{\partial x}\left(D_e^{eff}\frac{\partial}{\partial x}c_e\right) + \frac{1-t_+^0}{F}j^{Li}$	$\left.\frac{\partial c_e}{\partial x}\right\|_{x=0} = \left.\frac{\partial c_e}{\partial x}\right\|_{x=L} = 0$
Electrolyte phase charge conservation	$\frac{\partial}{\partial x}\left(k^{eff}\frac{\partial}{\partial x}\phi_e\right) + \frac{\partial}{\partial x}\left(k_D^{eff}\frac{\partial}{\partial x}\ln c_e\right) + j^{Li} = 0$	$\left.\frac{\partial \phi_e}{\partial x}\right\|_{x=0} = \left.\frac{\partial \phi_e}{\partial x}\right\|_{x=L} = 0$
Butler-Volmer Equation	$j^{Li} = a_s i_0\left[exp\left(\frac{\alpha_a F}{RT}\eta\right) - exp\left(-\frac{\alpha_c F}{RT}\eta\right)\right]$	
Overpotential Equation	$\eta = \phi_s - \phi_e - U$	
Voltage Output Equation	$V(t) = \phi_s(L,t) - \phi_s(0,t) - \frac{R_c}{A}I(t)$	

by Ramadass et al. [17] and Randall et al. [18]. Battery performance and aging are affected by the battery temperature [12] and temperature distribution within a cell pack [13]. Higher battery temperature reduces cell impedances [32] but increases the battery degradation and SEI layer growth [19, 29].

Battery management systems (BMS) are responsible for safe and efficient battery operation. A variety of battery models (full order models [4, 5, 10, 25], equivalent circuit models [11, 31], reduced order models [16, 22, 23, 27, 28, 30]) have been developed for battery voltage prediction and SOC estimation. Equivalent and reduced order models are suitable for real-time applications as they are computationally fast and sufficiently accurate. Prasad et al. [16] developed a linear, single particle model which was improved by Tanim et al. [27] by adding electrolyte dynamics resulting in the seventh order electrolyte Enhanced Single Particle Model (ESPM).

Room temperature may not always be a desired operating temperature for the minimum battery pack size and cost, and active temperature control can improve the battery pack size and performance [7, 29]. Garg et al. [8] investigated the effect of the battery temperature on resizing the battery pack for HEV applications and proposed a model-based approach to select a battery pack depending on the life and performance requirements. Garg et al. [9] further experimentally demonstrated how step-wise temperature increases whenever the battery voltage exceeds a voltage limit could increase the Battery pack life.

Battery pack life and performance are also affected by the capacity mismatch in parallel-connected cells. Capacity mismatch can result from manufactured cell variations, including non uniform materials, processing, self-discharge rates, and impedances or operating conditions such as nonuniform temperature distributions [3]. Cell capacity imbalance can cause voltages non uniformity and create unsafe operating conditions

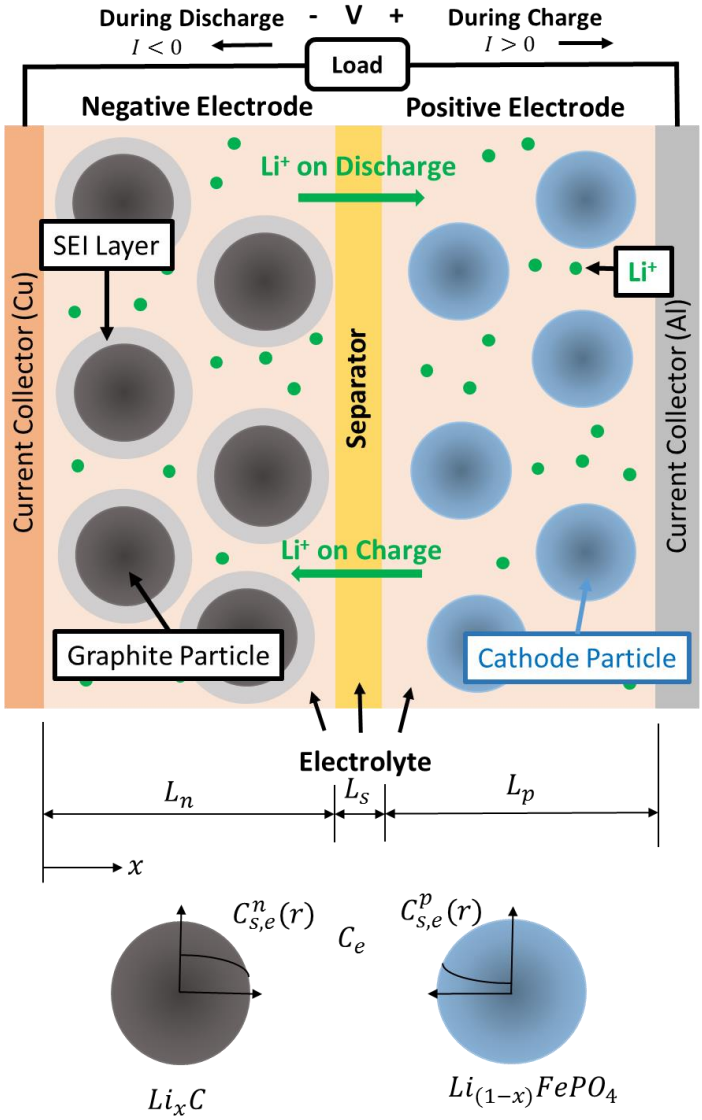

FIGURE 1: Schematic diagram of the pseudo-2D Li-ion battery model

such as battery overcharge. Cell balancing using fixed [14] or switching [2] shunt resistance can divert excess current and protect the cells from overcharge. This approach wastes energy that is dissipated as heat in the shunt resistance, reducing the efficiency of the pack. More complex and efficient active balancing methods using switched capacitors transport energy from higher energy cells to low energy cells [15, 24].

In this paper, temperature control for the reduction of battery pack capacity mismatch is studied through models and experiments. The ESPM model is extended to parallel-connected cells to calculate the current distribution in a battery pack. The model is augmented with SEI layer degradation to predict aging. The performance and aging predicted by the model are validated experimentally for parallel-connected cells of different capacities at different temperatures. Finally, a case study is presented to investigate temperature control that can simultaneously maximize the battery life and minimize the battery pack capacity mismatch.

2 Mathematical Modeling

Fig. 1 shows a schematic diagram of a pseudo-2D Li-ion battery model with three domains – negative electrode, separator, and positive electrode. The negative electrode typically has lithiated carbon as the active material while the positive electrode has a lithium metal oxide (e.g. NMC (Lithium Nickel Manganese Cobalt Oxide), LCO (Lithium Cobalt Oxide), LMO (Lithium Manganese Oxide) or LFP) as the active material. Lithium ions transport from the positive electrode to the negative electrode during charge (I<0) and the opposite direction during discharge (I>0). The anode and cathode reactions are, respectively,

$$Li_xC \underset{\text{charge}}{\overset{\text{discharge}}{\rightleftharpoons}} C + xLi^+ + xe^-,$$

$$Li_{(1-x)}FeO_4 + xLi^+ + xe^- \underset{\text{charge}}{\overset{\text{discharge}}{\rightleftharpoons}} LiFeO_4,$$

The separator allows lithium ions to diffuse through the cell but isolates the direct current path between the positive and negative electrodes. All three domains are saturated with electrolyte such as 1.2 M LiPF6 in ethylene carbonate (EC)/dimethyl carbonate (DMC). Thin aluminum and copper foils are connected as a current collectors for the positive and negative electrodes, respectively.

2.1 Single Battery Performance Model

Table 1 lists the fundamental governing equations of the pseudo-2D cell model. Four partial differential equations (solid phase charge conservation, solid phase ion conservation, electrolyte phase charge conservation, and electrolyte phase ion conservation) are coupled via the Butler-Volmer and overpotential equations. Reduced order battery models simplify these fundamental governing equations using assumptions and numerical model-order reduction tools. Reduced order models are accurate over a limited operating range, but they are computationally efficient.

Following Tanim et al. [27], a reduced order ESPM model is used. The models is a single particle model that assumes infinite solid phase conductivity and uniform temperature distribution

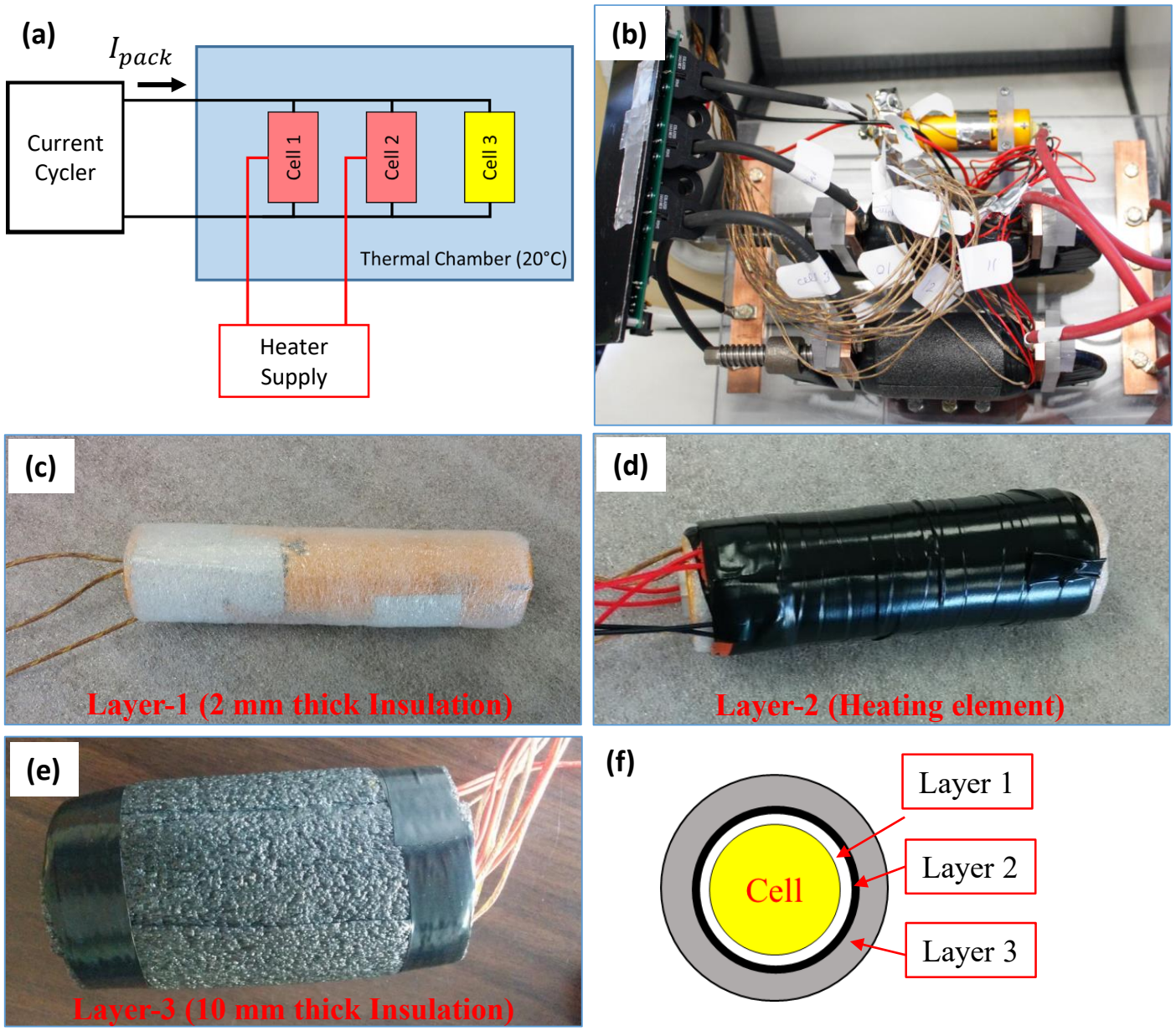

FIGURE 2: Three cells connected in parallel are placed in the thermal chamber. Cell 1 and 2 are insulated and heated using an external heater. Thermal chamber is kept at $20^{\circ}C$. (a) Schematic of the experimental setup, (b) Battery pack with Cell 3 without insulation, (c) Cell insulation layer 1, (d) Resistive heating element layer around the cell, (e) Another insulation layer over the resistive heater, and (f) cross section of the insulated cells.

across the cell. The model describes the voltage output for a single cell as follows:

$$\frac{V_{out}(s)}{I(s)} = \frac{\eta_p(s)}{I(s)} + \frac{\partial U}{\partial \tilde{C}^p_{s,e}} \frac{\tilde{C}^p_{s,e}}{I(s)} - \frac{\eta_n(s)}{I(s)} - \frac{\partial U}{\partial \tilde{C}^n_{s,e}} \frac{\tilde{C}^n_{s,e}}{I(s)} + \frac{\Delta\phi_e(L,s)}{I(s)} - \frac{R_c}{A} \quad (1)$$

Individual terms of the transfer function are described in [27]. The coefficients of the transfer function depend on the battery electrochemical and physical properties. The electrochemical properties are temperature dependent and the Arrhenius equation,

$$\psi = \psi_{ref} \exp\left[\frac{E_{act,\psi}}{R}\left(\frac{1}{R_{ref}} - \frac{1}{T}\right)\right], \tag{2}$$

is used for to calculate the temperature-dependent parameters. Table 2 lists the parameters for a single cell.

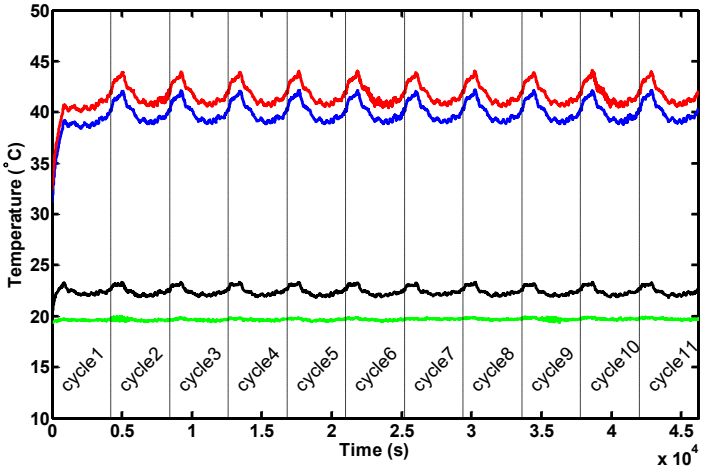

FIGURE 3: Experimental temperatures for the first 11 HEV cycles: Cell 1 (blue), Cell 2 (red), Cell 3 (black), and Thermal chamber (green) temperatures.

2.2 Battery Pack Performance Model

For a battery pack with three LFP cells connected in parallel, each cell has the same voltage V_{pack} and the battery pack current,

$$I_{pack} = I_{cell_1} + I_{cell_2} + I_{cell_3}, \tag{3}$$

is the sum of the cell currents. For a uniform pack, the cell currents are equal. In a non uniform pack, each cell has a different transfer function

$$G_{cell_1} = \frac{V_{pack}(s)}{I_{cell_1}(s)}, G_{cell_2} = \frac{V_{pack}(s)}{I_{cell_2}(s)}, G_{cell_3} = \frac{V_{pack}(s)}{I_{cell_3}(s)},$$

based on its capacity, parameters (e.g. internal resistance), and temperature.

TABLE 2: Model parameters of a 4.5 Ah LFP cell [26]

Parameter	Neg. electrode	Pos. electrode
Thickness, L (cm)	3.40×10^{-3}	7.00×10^{-3}
Particle radius, R_s (cm)	2.90×10^{-4}	3.65×10^{-6}
Active material volume fraction, ε_s	0.55	0.41
Exchange current density, $i_{0,ref}$ (A cm^{-2})	1.85×10^{-4}	8.18×10^{-5}
Charge transfer coefficient, α_a, α_c	0.5, 0.5	0.5, 0.5
Solid phase Li diffusion coefficient, $D_{s,ref}$ (cm^2 s^{-1})	5.29×10^{-11}	1.18×10^{-14}
Area, A (cm^2)	3580	3487

The individual cell current transfer functions can be calculated as:

$$\begin{aligned}
\frac{I_{cell_1}(s)}{I_{pack}(s)} &= \frac{G_T(s)}{G_{cell_1}(s)}, \\
\frac{I_{cell_2}(s)}{I_{pack}(s)} &= \frac{G_T(s)}{G_{cell_2}(s)}, \\
\frac{I_{cell_3}(s)}{I_{pack}(s)} &= \frac{G_T(s)}{G_{cell_3}(s)},
\end{aligned} \tag{4}$$

$$\text{where, } G_T(s) = \left(\frac{1}{G_{cell_1}} + \frac{1}{G_{cell_2}} + \frac{1}{G_{cell_3}}\right)^{-1},$$

2.3 Battery Pack Aging Model

Anodic overpotential for the intercalation/de-intercalation reaction for the i^{th} cell can be calculated using ESPM:

$$\frac{\eta_i(s)}{I_{cell_i}(s)} = \frac{R_{ct}^n}{a_s^n} \frac{1}{A_n L_n}$$

$$\eta_i = \phi_s^n - \phi_e - U_n(C_{s,e}^n)$$

Overpotential for SEI growth side reaction is

$$\eta^{sei} = \phi_s^n - \phi_e - U_{sei}^{ref}$$

Thus,

$$\eta_i^{sei} = \eta_i + U_n(C_{s,e}^n) - U_{sei}^{ref}$$

where U_{sei}^{ref} is 0.4V. The side reaction current for SEI layer growth and capacity loss of the individual cell are

$$j_i^{sei} = -a_s^n i_{0,sei} exp\left(-\frac{\alpha_n F}{RT}\eta_i^{sei}\right),$$

$$\frac{\partial Q_{LOSS_i}}{\partial t} = -j_i^{sei} A_n L_n,$$

where Q_{LOSS_i} is the capacity loss in the i^{th} cell due to the SEI layer growth.

3 Experiment Setup

Three LFP cylindrical cells are connected in parallel to construct the battery pack shown schematically and in a photograph in Fig. 2. The battery pack is placed in a thermal chamber to control the environmental temperature. An Arbin cycler charges and discharges the battery pack using a predefined HEV cycle. The Arbin also measures the battery pack voltage and current. Cell 1 and Cell 2 are insulated and heated using a resistive heater, so they operate at higher temperature than Cell 3. The mean temperatures of Cell 1, 2, and 3 are 39.5°C, 42°C, and 23°C, respectively. Hall Effect current sensors measure the current in the individual cells. Fig. 3 shows the temperature of different cells and environmental chamber for the first 11 HEV cycles. The system reaches steady state within a couple of 4200s long HEV cycles.

The battery pack is cycled for 1500 HEV cycles and capacity is measured roughly every 250 cycles. Cell capacity is measured as follows: (1) Charging to 3.6 V at 1C constant current; (2) Holding voltage constant at 3.6 V until the current drops to C/20; (3) Resting for 30 min; and (4) Discharging at 1C rate to a cut-off voltage of 2.0 V. The initial capacities of Cell 1, 2 and 3 are 4.27Ah, 4.27Ah, and 3.98Ah, respectively.

4 Experimental Results and Discussion

4.1 Current Distribution

Fig. 4 shows the experimental and simulated current in Cell 2 and 3 at the beginning of the cycling and after 1300 HEV cycles. The theory and experiment match extremely well, indicating the accuracy of proposed performance and aging models. Table 3 shows the maximum error in RMS current is around 1% for the aged cell.

As expected, the current distribution is very sensitive to cell temperature, with higher temperature cells taking more current. Table 3 shows the RMS currents in the three cells, Cell 1 and 2 are roughly $18°C$ warmer than Cell 3 and they take almost 33% more current. Even the small temperature difference of $2°C$ between Cells 1 and 2 results in 0.5A more current going to the hotter cell 2. The experimentally observed temperature difference between Cell 1 and 2 may be due to insulation and internal heat generation variations between two cells.

TABLE 3: Summary of the test results

	Cell No.	Initial Values before cycling	Final values after 1300 HEV cycles
Capacity (Ah)	1	4.27	4.27
	2	4.27	4.00
	3	3.98	3.88
Temperature (°C)	1	40.08	39.68
	2	41.88	41.92
	3	22.45	23.14
Exp. RMS Current (A)	1	29.14	28.87
	2	29.52	29.42
	3	20.21	20.23
Error in RMS current (%)	1	0.69	1.03
	2	-0.49	-0.02
	3	0.28	-1.00

The current distribution is relatively insensitive to cell capacity variation. Fig. 4 and Table 3 show almost identical current distribution at the beginning and end of the test, even though the cell capacities are much closer at the end of the test.

4.2 Capacity Fade

Fig. 5 shows that the cell capacity loss mirrors the current distribution. The hottest Cell 2 degrades the quickest and the coolest Cell 3 maintains its capacity. The model predictions of capacity are not as accurate as performance. This is partially due to the capacity measurement inaccuracies. Accurate aging prediction also requires consideration of alternative aging mechanisms (e.g. electrode cracking). This may explain why the aging model under predicts capacity loss.

4.3 Mismatch Reduction Through Different Temperature Control

Fig. 5 shows that the rate of capacity fade for Cell 1 and 2 is much higher than the rate of capacity fade for Cell 3 due to their higher temperature. The battery pack used for the experiment is not uniform with cell capacity varying by as much as 7.45% at the beginning of the test. The non uniform temperature distribution causes differential aging so the battery pack becomes more uniform over time. Thus, temperature control has been demonstrated to reduce capacity mismatch in parallel-connected LFP batteries. The capacity of each cell is measured separately

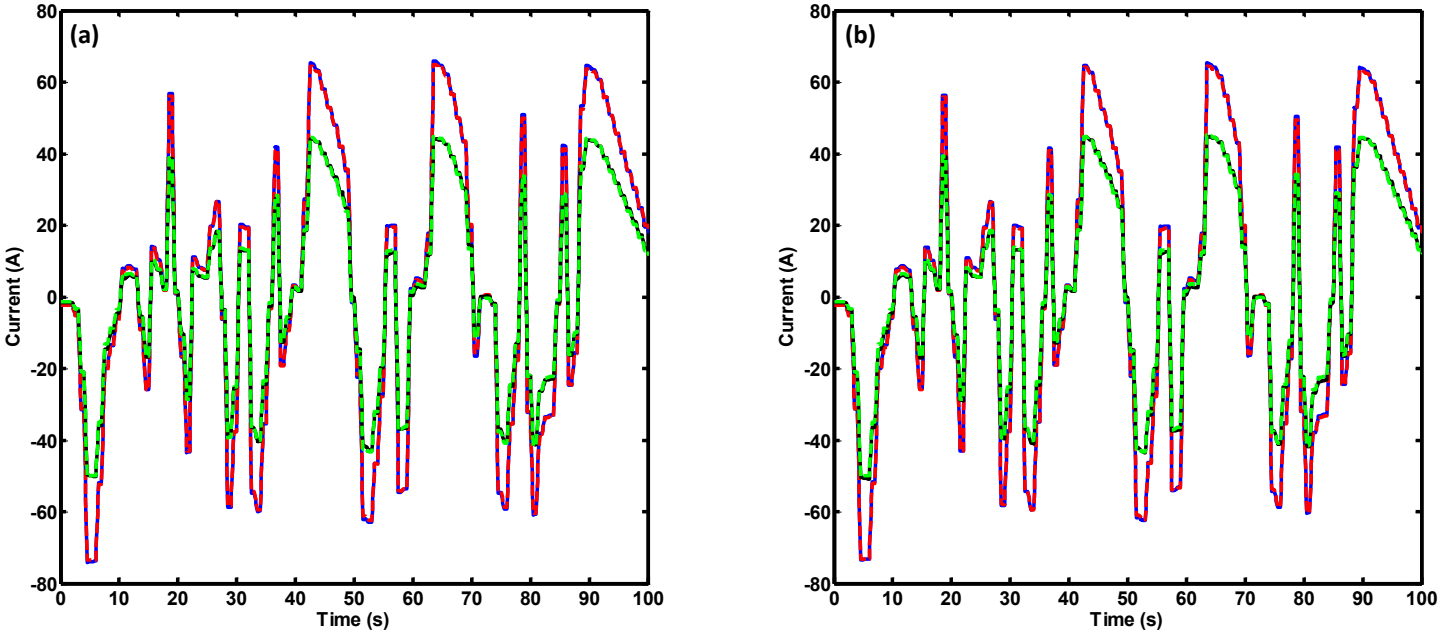

FIGURE 4: Current distributions in Cells 2 and 3 initially (a) and after 1300 HEV cycles (B): Experimental current in cell 2 (red dashed) and cell 3 (green dashed); simulated current in cell 2 (blue solid) and cell 3 (black solid). The capacity, current, and prediction error of each cell are listed in Table 3. Results from Cell 1 are not shown to ensure figure clarity and because they are very close to Cell 2.

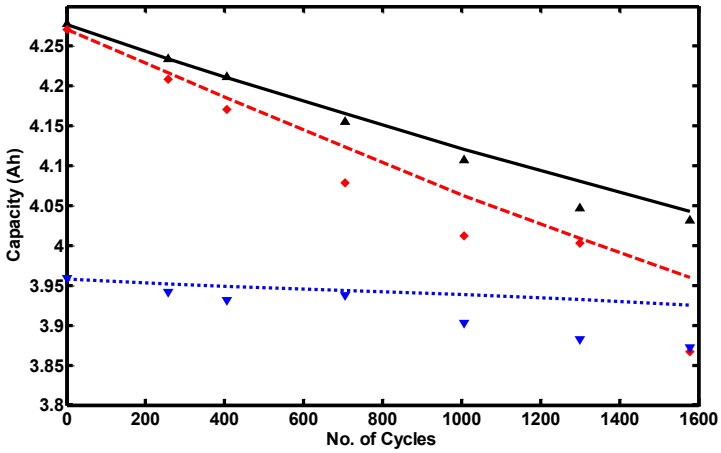

FIGURE 5: Experimental validation of the battery capacity fade model for cells (1-3) at mean cycle temperatures of 39.5°C, 43°C, and 23°C and initial capacities of 4.27Ah, 4.27 Ah, and 3.98Ah, respectively. Simulated capacity fade: Cell 1 (black solid line), Cell 2 (red dashed line), and Cell 3 (blue dotted line). Experimental capacity fade: Cell 1 (black upward-pointing triangle), Cell 2 (red diamond), and Cell 3 (blue downward-pointing triangle).

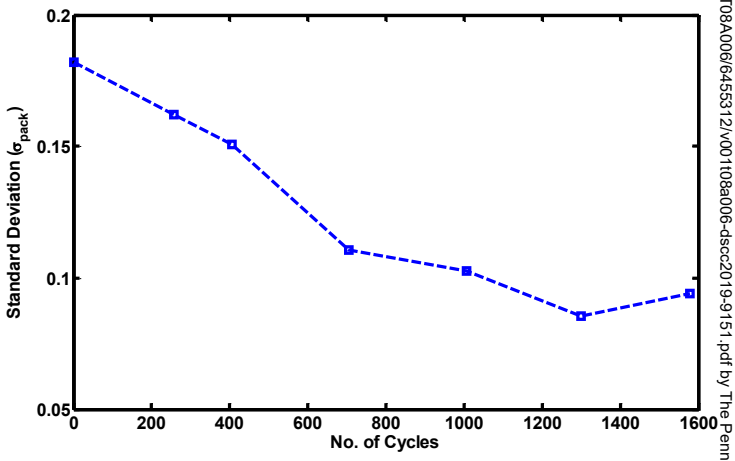

FIGURE 6: Experimentally measured cell capacities standard deviation versus number of cycles.

at 25°C at different intervals.

Fig. 6 shows the standard deviation of the cell capacities σ_{pack} versus time. The pack capacities converge as the experiment progresses, resulting in a 48% reduction in σ_{pack}.

TABLE 4: Case Study Results

Case #	Battery Pack Life (Years)	Mismatch Reduction (%)	Cooling Energy
Case 1	2.09	10	None
Case 2	4.70	10	Highest
Case 3	3.52	100	Less than case 2
Case 4	4.71	100	Less than case 2, more than case 3

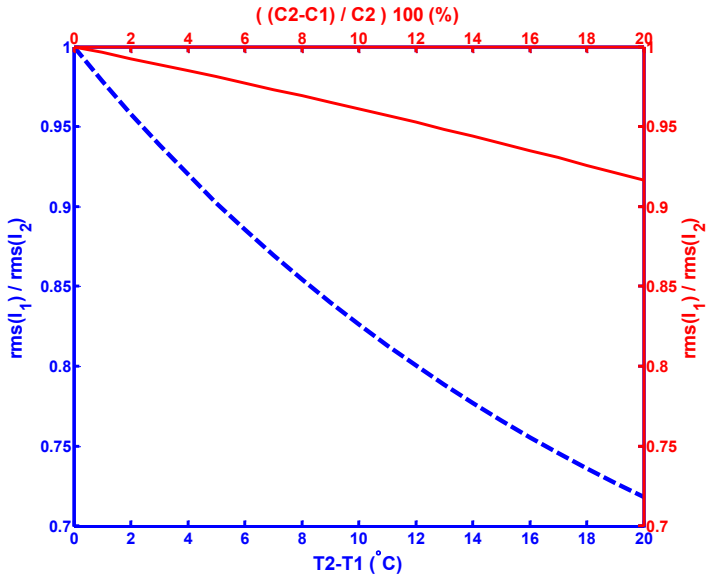

FIGURE 7: Ratio of current RMS versus temperature (blue dashed) and capacity (red solid) mismatch in a battery pack with two cells connected in parallel.

5 Temperature control for simultaneous life maximization and capacity balance

The experimental results confirm theoretical predictions that differential temperature can be used to balance the capacity of parallel-connected cells. Using the validated model, it was further investigated whether temperature control can simultaneously balance capacity and extend the life of these packs.

Fig. 7 shows the sensitivity of the current distribution to temperature and capacity mismatch. As observed in the experiment, the current distribution is much more sensitive to temperature mismatch than capacity mismatch. Thus, relying on the natural self-balancing of the capacity mismatch may not be sufficient to counter unbalancing effects. Temperature difference, however, can significantly accelerate balancing, with 20°C causing almost 30% increase in differential current. Higher temperatures also accelerate aging so cooling the lower capacity cell has the potential to accelerate capacity balancing and extend pack life.

For simplicity, consider a battery pack with two cells connected in parallel, current distribution transfer functions (Eq. 4) simplify to

$$\frac{I_{cell_1}(s)}{I_{pack}(s)} = \frac{G_{cell_2}(s)}{G_{cell_1}(s)+G_{cell_2}(s)}$$

$$\frac{I_{cell_2}(s)}{I_{pack}(s)} = \frac{G_{cell_1}(s)}{G_{cell_1}(s)+G_{cell_2}(s)}$$

Case study parameters: Four cases are studied to quantify the effect of temperature on capacity mismatch and life. For all four cases one cell start at 4.3Ah and the other at 4.0Ah. End of life (EOL) is defined as when one cell reaches 80% of the fresh cell capacity (4.5Ah). Environmental temperature is 30°C. The four cases:

Case 1: Both batteries are operated at the environmental temperature ($30°C$) until battery pack EOL.

Case 2: Both batteries are cooled to operate at room temperature ($25°C$) until battery pack EOL.

Case 3: Cell 1 and 2 are operated at environmental and room temperature, respectively, until both cells have the same capacity. Then, both cells are operated at the environmental temperature until EOL.

Case 4: Cell 1 and 2 are operated at environmental and room temperature, respectively, until both cells have the same capacity. Then, both cells are operated at the room temperature until EOL.

In each case, a continuous UDDS cycle is the battery current input. The battery pack performance and degradation model, validated in the experimental study, are used to quantify the capacity mismatch evolution and capacity fade.

Fig. 8 shows the simulated capacity change of the individual cell versus time for the four cases. In Case 1 and 2, both batteries

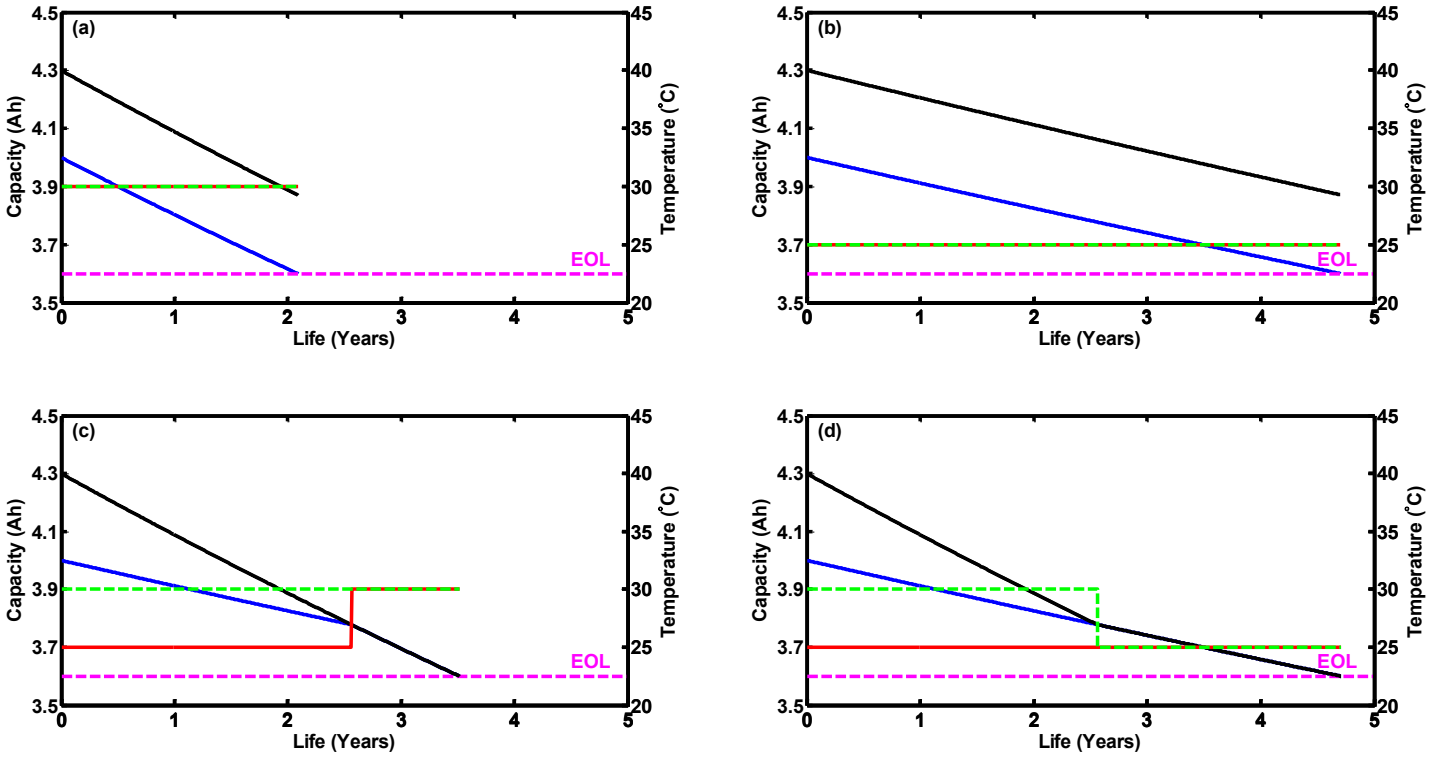

FIGURE 8: Simulated battery capacity change in Case 1 (a), Case 2 (b), Case 3 (c), and Case 4 (d). Cell 1 capacity fade (black solid line), Cell 2 capacity fade (blue solid line), Cell 1 temperature (green solid line), and Cell 2 temperature (red dashed line). EOL at 3.6Ah is marked by the magenta dashed line.

degrade at a similar rate, but the rate of degradation of the battery pack is higher in case 1. In both cases, capacity mismatch narrows by roughly 10%. This reduction is solely due to the current redistribution caused by the capacity mismatch because both cells have the same temperature. If the temperature is low, the overall capacity fade rate is less, resulting in 4.70 years versus 2.1 years of life for Case 2 and 1, respectively. In Case 3 and 4, the lower capacity battery is cooled at room temperature until both batteries have the same capacity. Cell 1 degrades more slowly and their capacities converge over time. In case 3, both batteries are kept at the higher, environmental temperature after capacity is matched. This increases the degradation rate of the battery pack, reducing pack life compare to Case 4. Table 4 summarizes the findings of the case study.

Battery capacity mismatch has less impact on the current distribution and battery capacity fade, so self-balancing is not effective and temperature control is required to balance the battery pack before EOL. In isothermal Cases 1 and 2, the capacity mismatch is only reduced by 10%. Case 4 is the best for maximum battery life and capacity mismatch reduction with moderate energy consumption for battery pack cooling.

6 Conclusion

The paper develops and validates a battery performance and aging model for parallel-connected cells. The model predicts the capacity evolution within 0.60% over 1500 HEV cycles. The experimental results show that around 18°C temperature difference can reduce the capacity mismatch by 48% over 1500 HEV cycles. Finally, differential cooling of parallel-connected cells can reduce capacity mismatch and extend pack life.

ACKNOWLEDGMENT

The authors greatly appreciate Volvo Group Trucks Technology for financially supporting this project.

REFERENCES

[1] Vehicle Technologies Office: Moving America Forward With Energy Efficient Vehicles. "https://energy.gov/eere/vehicles/vehicle-technologies-office-0", 2008. [Online; accessed 13-June-2017].

[2] Dorin V Cadar, Dorin M Petreus, and Toma M Patarau.

In *33rd International Spring Seminar on Electronics Technology, ISSE 2010*, pages 290–293. IEEE, 2010.

[3] Mohamed Daowd, Noshin Omar, Peter Van Den Bossche, and Joeri Van Mierlo. *J. Int. Rev. Electr. Eng*, 6:2974–2989, 2011.

[4] M Doyle and Y. Fuentes. *J. Electrochem. Soc.*, 150(6):A706–A713, 2003.

[5] M. Doyle and J. Newman. *J. Electrochem. Soc.*, 143(6):1890–1903, 1996.

[6] A. Eddahech, O. Briat, and J. Vinassa. *Energy*, 84:542–550, 2015.

[7] Mayank Garg and Christopher Rahn. Technical report, SAE Technical Paper, 2017.

[8] Mayank Garg and Christopher D Rahn. In *American Control Conference (ACC), 2017*, pages 4159–4164. IEEE, 2017.

[9] Mayank Garg, Tanvir R Tanim, Christopher D Rahn, Hanna Bryngelsson, and Niklas Legnedahl. *Energy*, 159:716–723, 2018.

[10] W. B. Gu and C. Y. Wang. *J. Electrochem. Soc.*, 147(8):2910–2922, 2000.

[11] H. He, X. Zhang, R. Xiong, Y. Xu, and H. Guo. *Energy*, 39(1):310–318, 2012.

[12] J Jaguemont, L Boulon, and Y Dubé. *Applied Energy*, 164:99–114, 2016.

[13] M Klein, S Tong, and JW Park. *Applied Energy*, 165:639–647, 2016.

[14] Nasser H Kutkut and Deepak M Divan. In *Telecommunications Energy Conference, 1996. INTELEC'96., 18th International*, pages 514–521. IEEE, 1996.

[15] Cesar Pascual and Philip T Krein. In *Applied Power Electronics Conference and Exposition, 1997. APEC'97 Conference Proceedings 1997., Twelfth Annual*, volume 2, pages 848–854. IEEE, 1997.

[16] Githin K Prasad and Christopher D Rahn. In *ASME 2012 5th Annual Dynamic Systems and Control Conference joint with the JSME 2012 11th Motion and Vibration Conference*, pages 369–375. American Society of Mechanical Engineers, 2012.

[17] P. Ramadass, B. Haran, P. M. Gomadam, R. White, and B. N. Popov. *J. Electrochem. Soc.*, 151(2):A196–A203, 2004.

[18] Alfred V Randall, Roger D Perkins, Xiangchun Zhang, and Gregory L Plett. *Journal of Power Sources*, 209:282–288, 2012.

[19] M. Safari and C. Delacourt. *J. Electrochem. Soc.*, 158(10):A1123–A1135, 2011.

[20] M. Safari and C. Delacourt. *J. Electrochem. Soc.*, 158(12):A1436–A1447, 2011.

[21] E. Sarasketa-Zabala, I. Gandiaga, L.M. Rodriguez-Martinez, and I. Villarreal. *J. of Power Sources*, 272:45–57, 2014.

[22] Kandler A Smith, Christopher D Rahn, and Chao-Yang Wang. *Journal of Dynamic Systems, Measurement, and Control*, 130(1):011012, 2008.

[23] Kandler A Smith, Christopher D Rahn, and Chao-Yang Wang. *IEEE Transactions on Control Systems Technology*, 18(3):654–663, 2010.

[24] Carmelo Speltino, Anna Stefanopoulou, and Giovanni Fiengo. In *Proceedings of the 2010 American Control Conference*, pages 5050–5055. IEEE, 2010.

[25] V. Srinivasan and J. Newman. *J. Electrochem. Soc.*, 151:A1517–A1529, 2004.

[26] Tanvir R Tanim and Christopher D Rahn. *Journal of Power Sources*, 294:239–247, 2015.

[27] Tanvir R Tanim, Christopher D Rahn, and Chao-Yang Wang. *Journal of Dynamic Systems, Measurement, and Control*, 137(1):011005, 2015.

[28] Tanvir R Tanim, Christopher D Rahn, and Chao-Yang Wang. *Energy*, 80:731–739, 2015.

[29] Tanvir R Tanim, Matthew G Shirk, Randy L Bewley, Eric J Dufek, and Bor Yann Liaw. *Journal of Power Sources*, 381:56–65, 2018.

[30] Tanvir R Tanim, Christopher D Rahn, and Chao-Yang Wang. In *2014 American Control Conference*, pages 141–146. IEEE, 2014.

[31] M. Verbrugge and P. Liu. *J. Power Sources*, 174(1):2–8, 2007.

[32] Wladislaw Waag, Stefan Käbitz, and Dirk Uwe Sauer. *Applied Energy*, 102:885–897, 2013.